Angular Dispersions in Terahertz Metasurfaces: Physics and Applications

Meng Qiu,[1,*] Min Jia,[1,*] Shaojie Ma,[1] Shulin Sun,[2] Qiong He,[1,3,†] and Lei Zhou[1,3,‡]

[1]*State Key Laboratory of Surface Physics, Key Laboratory of Micro and Nano Photonic Structures (Ministry of Education), and Department of Physics, Fudan University, Shanghai 200433, China*

[2]*Shanghai Engineering Research Center of Ultra-Precision Optical Manufacturing, Green Photonics and Department of Optical Science and Engineering, Fudan University, Shanghai 200433, China*

[3]*Collaborative Innovation Center of Advanced Microstructures, Nanjing 210093, China*

(Received 11 March 2018; published 31 May 2018)

Angular dispersion—the response of a metasurface strongly depending on the impinging angle—is an intrinsic property of metasurfaces, but its physical origin remains obscure, which hinders its applications in metasurface design. We establish a theory to *quantitatively* describe such intriguing effects in metasurfaces, and we verify it by both experiments and numerical simulations on a typical terahertz metasurface. The physical understanding gained motivates us to propose an alternative strategy to design metadevices exhibiting impinging-angle-dependent multifunctionalities. As an illustration, we design a polarization-control metadevice that can behave as a half- or quarter-wave plate under different excitation angles. Our results not only reveal the physical origin of the angular dispersion but also point out an additional degree of freedom to manipulate light, both of which are important for designing metadevices facing versatile application requests.

DOI: 10.1103/PhysRevApplied.9.054050

I. INTRODUCTION

Metasurfaces are planar metamaterials composed of subwavelength microunits (e.g., "meta-atoms") with tailored electromagnetic (EM) properties [1,2]. Many fascinating wave-manipulation effects have been discovered based on carefully designed periodic [3–19] or inhomogeneous gradient metasurfaces [20–27], such as polarization control [3–8], perfect absorption [9–12], tunneling-induced transparency [14–16], anomalous reflection or refraction [20,21], propagating-wave-to-surface-wave conversion [22,23], and other interesting effects [13,17–19,24–27]. The functional devices realized based on these fascinating effects are thin, flat, and highly efficient, making them favorable for integration-optics applications.

In designing these metasurfaces, a commonly adopted approach is to utilize the EM properties (i.e., amplitude and/or phase of transmission and/or reflection) of meta-atoms under normal-incidence excitations. However, in certain cases, the EM response of a metasurface may change dramatically as the excitation angle varies—a phenomenon usually called *angular dispersion*, as schematically depicted in Figs. 1(a) and 1(b). In practical metasurface design, scientists have usually made great effort to avoid such an effect by seeking structures with weak angular dispersions [9,12,28–32]. However, the intrinsic physics underlying this intriguing behavior has not been adequately investigated; thus, scientists usually rely on brute-force simulations to search for structures exhibiting weak angular dispersions. Knowing little about how to manipulate the angular dispersion of metasurfaces, scientists certainly cannot utilize it in metasurface design.

In this paper, we show that the angular dispersion of a metasurface is dictated by the plasmonic couplings among meta-atoms inside the structure, and we further establish a theory to *quantitatively* analyze such behaviors in periodic metasurfaces by extending the photonic tight-binding method (TBM) developed previously for few-resonator systems [33] to the present periodic systems. Our theory is validated by both experiments and full-wave simulations on a typical periodic terahertz metasurface, which exhibits intriguingly *opposite* angular dispersions for oblique incident waves taking transverse-electric (TE) or transverse-magnetic (TM) polarizations. The physics gained through analyzing these fascinating effects motivates us to propose an alternative strategy to design a multifunctional metadevice; that is, we can control the angular dispersion of a metasurface such that it can function distinctly when "seen" at different incident angles. As a proof of concept, we design a bifunctional metadevice that exhibits distinct polarization-control capabilities for incident beams coming from different angles [see Figs. 1(c) and 1(d)]. Our findings can help us to understand and manipulate the angular

*These authors contributed equally to this work.
†Corresponding author.
qionghe@fudan.edu.cn
‡Corresponding author.
phzhou@fudan.edu.cn

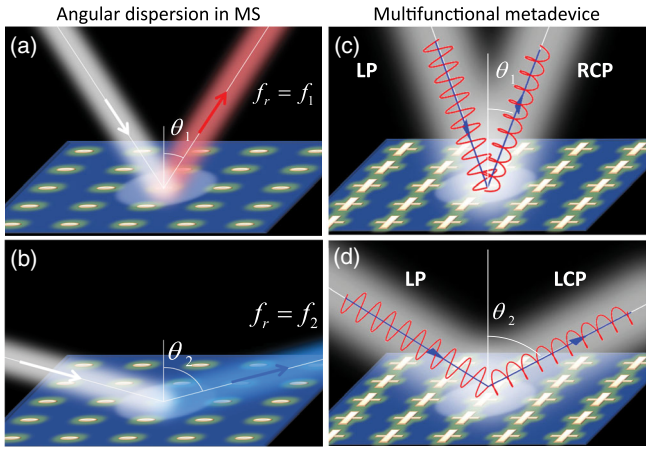

FIG. 1. (a),(b) Manifestation of angular dispersion in metasurfaces (MS) represented by resonant frequency shift ($f_1 \neq f_2$) of a metasurface seen at different incidence angles ($\theta_1 \neq \theta_2$). (c),(d) Schematics of an incident-angle-dependent multifunctional metadevice for polarization control on a reflective beam. Here, the metadevice can convert a linearly polarized (LP) wave to a right-handed (RCP) or left-handed circular-polarized (LCP) wave under different incidence angles.

dispersions of metasurfaces, which can significantly expand our capabilities of designing metasurface-based functional devices.

II. ANGULAR DISPERSIONS OF A TERAHERTZ METASURFACE: EXPERIMENTAL RESULTS

We start by experimentally characterizing the rich angular-dispersion behaviors of a typical terahertz metasurface, consisting of a periodic array of subwavelength metallic split-ring resonators (SRRs) on a dielectric substrate [see Fig. 2(a) for the sample picture]. The reason that we choose SRR as our meta-atom is that a SRR exhibits very intriguing EM responses [34–36], leading to rich coupling effects between two such meta-atoms, as has already been demonstrated in Refs. [33,37,38]. Specifically, at its lowest resonance, a SRR exhibits a magnetic dipole moment ($\vec{m}$) perpendicular to its plane as well as an electrical dipole moment ($\vec{p}$) along an in-plane direction dictated by the gap position. As a result, we expect that a metasurface formed by such meta-atoms should exhibit very rich angular dispersions, sensitively depending on the orientation angle α of the SRR gap. Therefore, we purposely fabricate a series of terahertz metasurfaces following standard photolithography procedures, in which the SRRs possess identical geometrical parameters (see the caption of Fig. 1) but with different orientation angles ($\alpha = 0°$, 15°, 30°, 45°, 60°, 75°, and 90°). In all of these samples (all exhibiting a total size of 1×1 cm^2), the metallic structures are made with a 60-nm-thick Au film plus a 5-nm-thick Cr film as adhesion layer, and they are deposited on 500-μm-thick quartz substrates.

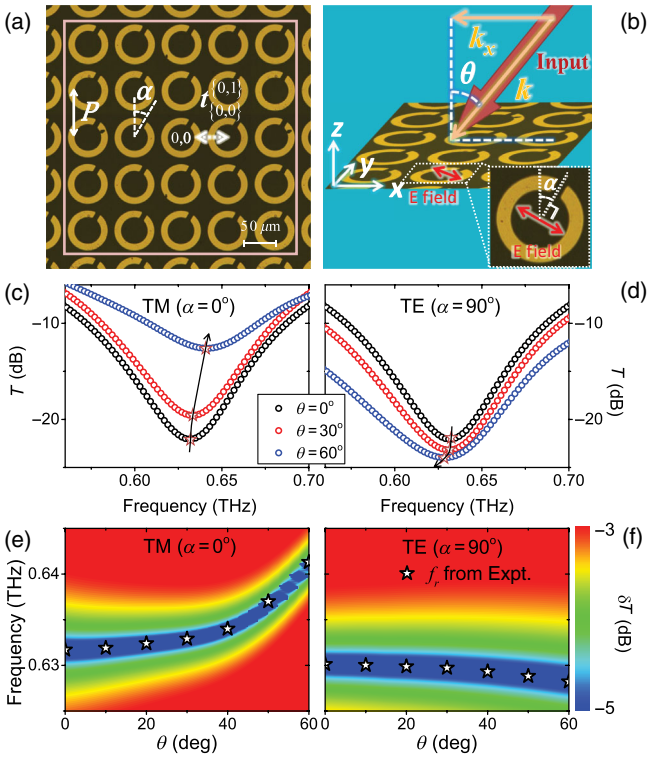

FIG. 2. (a) Optical picture of part of the fabricated terahertz metasurface sample. (b) Schematics of our experimental characterizations on angular dispersion of the terahertz samples. The incident light lies in the x-z plane, while the in-plane **E** field is polarized along the direction, as shown in the inset. (c),(d) Measured (scatter) transmittance spectra of the metasurfaces with different incident angles for the TM ($\alpha = 0°$) and TE ($\alpha = 90°$) polarizations, respectively. (e),(f) Computed rescaled transmittance δT (color map) of two metasurfaces (with $\alpha = 0°$ and $\alpha = 90°$) versus the frequency and incident angle, with stars representing the measured resonant-mode positions. Geometrical parameters of the SRR: inner and outer radius, $R_1 = 20$ μm and $R_2 = 30$ μm; gap width, $g = 6$ μm. Lattice constant of the array, $P = 70$ μm.

We characterize the angular dispersions of these fabricated metasurfaces by measuring their transmittance spectra at different incident angles θ, using a terahertz time-domain spectroscopy. As is schematically depicted in Fig. 2(b), in order to correctly and efficiently excite the resonant modes in SRRs and make fair comparisons between samples with different values of α, we purposely set the in-plane component of the incident **E** field strictly parallel to the intrinsic $\vec{p}$ moments possessed by the SRRs [see the inset in Fig. 2(b)], and we vary the incident **k** vector within the x-z plane to measure the corresponding transmittance spectra at different incident angles. Obviously, our experimental configuration corresponds to the TM (TE) excitation for the sample with $\alpha = 90°$ ($\alpha = 0°$). For other samples with arbitrary α values, our measurements do not correspond to any well-defined TE or TM excitation, but the obtained transmittance spectra still

contain all necessary information on the angular dispersions as long as the "modes" in different metasurfaces are correctly excited. All measured transmittance signals are normalized against a reference signal, obtained under exactly the same excitation configuration, only with the sample replaced by a quartz substrate of the same thickness. The multiple scatterings of terahertz waves inside the substrate are purposely excluded in our measurements through a standard time-domain cutoff procedure.

Figures 2(c) and 2(d) compare, respectively, the transmittance spectra of two representative samples (with $\alpha = 0°$ and $\alpha = 90°$) measured at different incident angles θ. The excited resonance mode exhibits a clear frequency shift as we vary θ for the two studied samples (see experimental results for other samples in the Supplemental Material [39]). Surprisingly, we note that the two metasurfaces display opposite angular dispersions manifested by different signs of frequency shift. Specifically, whereas the $\alpha = 0°$ metasurface exhibits a blueshift of resonant frequency as θ increases [Fig. 2(c)], the $\alpha = 90°$ metasurface exhibits a redshift of resonant frequency [Fig. 2(d)]. Further noting the rotation symmetry between the two samples, we draw an interesting conclusion that such a metasurface exhibits opposite angular dispersions when seen at different polarizations (TE or TM). Such an intriguing behavior has rarely been noted in the literature.

All experimental results are verified by full-wave simulations on realistic metasurface structures based on finite-element-method (FEM) simulations [40]. The solid lines in Figs. 2(c) and 2(d) are FEM-simulated transmittance spectra for different cases, which are all in reasonable agreement with their experimental counterparts. Slight discrepancies between experiments and simulations might be caused by sample imperfections. To see the comprehensive angular-dispersion behaviors, we plot in Figs. 2(e) and 2(f) the FEM-simulated transmittance versus frequency and incident angle for TM- and TE-polarization excitations, respectively. To increase the contrast, we purposely show in Figs. 2(e) and 2(f) the transmittance difference, $\delta T = T - T_{\mathrm{res}}$, with T_{res} being the computed transmittance at resonance (i.e., the minimum transmittance) inside every spectrum. The positive and negative angular dispersions of the metasurface under different excitations are clearly observed to be in excellent agreement with the experimentally measured transmittance-dip positions represented by the symbols. Again, more FEM and experimental results can be found in the Supplemental Material [39] for other cases studied.

III. THEORETICAL ANALYSES OF ANGULAR DISPERSIONS IN METASURFACES

We now establish a theoretical framework to quantitatively understand the intriguing angular dispersion behaviors experimentally revealed in the last section. According to the Hamiltonian formalism established previously for dispersive photonic systems [41], we understand that a single resonator (SRR here) exhibits a plasmonic resonance at a certain frequency f_0 with well-defined EM wave functions $|\Phi_s(\vec{r})\rangle = \{\vec{E}(\vec{r}), \vec{H}(\vec{r})\}$. When more plasmonic resonators are placed together, the modes associated with these resonators will couple with each other. According to the photonic TBM established [33], we can explicitly calculate the coupling strength between any two resonators via the following formula,

$$t_{\{m,n\}}^{\{k,l\}} = -f_0 \frac{\int \vec{P}^*_{\{m,n\}}(\vec{r}) \cdot \vec{E}_{\{k,l\}}(\vec{r}) d\tau}{\langle \Phi_s | \Phi_s \rangle}, \tag{1}$$

where $\vec{P}_{\{m,n\}}(\vec{r})$ denotes the polarization field inside the meta-atom located at the lattice site $\mathbf{R}_{\{m,n\}}$, while $\vec{E}_{\{k,l\}}(\vec{r})$ denotes the $\mathbf{E}$-field distribution generated by the meta-atom located at the lattice site $\mathbf{R}_{\{k,l\}}$, and $\langle \Phi_s | \Phi_s \rangle$ is the normalization constant representing the total EM-field energy stored in a single meta-atom. The validity of such a theory was well justified in Ref. [33] for few-resonator plasmonic systems. In particular, the TBM can precisely predict the frequencies of the hybridized modes in a two-resonator system, with all parameters calculated directly from Eq. (1) without any fitting procedures.

We now extend the TBM for few-resonator system to present *periodic* metasurface system. In metasurfaces where meta-atoms are placed in a two-dimensional periodic lattice, any meta-atom can interact with others via the coupling strengths defined in Eq. (1). As a result, couplings among these meta-atoms generate a branch of "collective" modes labeled by the Bloch $\mathbf{k}$ vector. Following the standard procedure in solid-state physics [42], we find that the eigenfrequency of a collective mode labeled by a Bloch $\mathbf{k}$ vector is

$$f(\mathbf{k}) = f_0 + \sum_{m,n} t_{\{0,0\}}^{\{m,n\}} \cos\left[\mathbf{k} \cdot \left(\mathbf{R}_{\{m,n\}} - \mathbf{R}_{\{0,0\}}\right)\right], \tag{2}$$

where $\mathbf{R}_{\{0,0\}}$ is the position of a reference meta-atom, while the summation runs over all neighboring meta-atoms that can have non-negligible couplings with the reference one. Obviously, the coupling strength decays as the distance between the two resonators is enlarged. We can consider only a finite number of meta-atoms near the reference one, depending on the quality (Q) factor of the single-particle resonance. Since a higher Q factor indicates that the wave function of the resonance mode is more localized around the meta-atom, fewer interparticle coupling terms are needed to obtain a convergent result. In the present case, where the single-particle resonance exhibits a relatively low Q factor, we consider the couplings between the central meta-atom and the other meta-atoms in a 5×5 square [the region surrounded by the pink lines in Fig. 2(a)], in order to make our TBM calculations convergent. We also perform TBM calculations by considering the couplings between all

meta-atoms in a 3×3 square and in a 7×7 square. The former exhibits huge deviations from the full-wave simulations, while the latter shows a slight improvement compared to the calculations based on a 5×5 square.

With all involved parameters $t_{\{0,0\}}^{\{m,n\}}$ computed from the TBM based on Eq. (1) [43,44], we next use Eq. (2) to calculate the dispersion relation $f(\mathbf{k})$ of the collective mode in different periodic metasurfaces. Noting that an incident wave can only excite a collective mode with a *matched* in-plane $\mathbf{k}$ vector, we understand that the dip frequency of the measured or calculated transmittance spectrum at the oblique incidence θ must be the frequency of the collective mode with the correct Bloch $\mathbf{k}$ vector. Putting $\mathbf{k} = \hat{x}k_0 \sin\theta$ (k_0 is the free-space wave vector of incident light) into the computed $f(\mathbf{k})$ function, we can thus predict how the transmittance-dip frequencies vary against the incident angle for different metasurfaces.

The angular dispersions $f(\theta)$ calculated with the TBM for different samples are shown in Fig. 3(a) as dashed lines, which are in nice agreement with experimental (stars) and FEM results (solid lines). In particular, our TBM results correctly reproduce the intriguing sign-change behavior of the angular dispersion as α decreases, and the critical value of α is found to be around 60°. We note that the agreement between TBM and FEM is better for systems exhibiting weaker angular dispersion, which is reasonable since we consider only the coupling terms inside the 5×5 array. By taking more coupling terms into account, more accurate results are expectable for the system with stronger angular dispersion.

To further understand why different metasurfaces exhibit distinct angular dispersions, we simplify Eq. (2) as follows:

$$f(\theta) = f_0 + J_0 + J_1 \cos(Pk_0 \sin\theta) + J_2 \cos(2Pk_0 \sin\theta), \tag{3}$$

where P is the lattice constant, J_0 denotes the effective intrarow coupling, while J_1 and J_2 denote the nearest-neighbor and next-nearest-neighbor effective intrarow couplings. These *effective* coupling coefficients are related to the interparticle coupling strengths via

$$J_0 = \sum_{i=-2}^{2} t_{\{0,0\}}^{\{i,0\}}, \quad J_1 = 2\sum_{i=-2}^{2} t_{\{0,0\}}^{\{i,1\}}, \quad J_2 = 2\sum_{i=-2}^{2} t_{\{0,0\}}^{\{i,2\}}. \tag{4}$$

Obviously, J_0 does *not* contribute to the angular dispersion under our experimental configuration, but J_1 and J_2 must make important contributions. Now both $\cos(Pk_0 \sin\theta)$ and $\cos(2Pk_0 \sin\theta)$ are decreasing functions of θ in the small-θ regime, Eq. (3) tells us that the signs of J_1 and J_2 dictate the angular dispersions of the metasurfaces under study. Specifically, the resonance dip must undergo a blueshift as θ increases if J_1 and J_2 are negative, and vice versa.

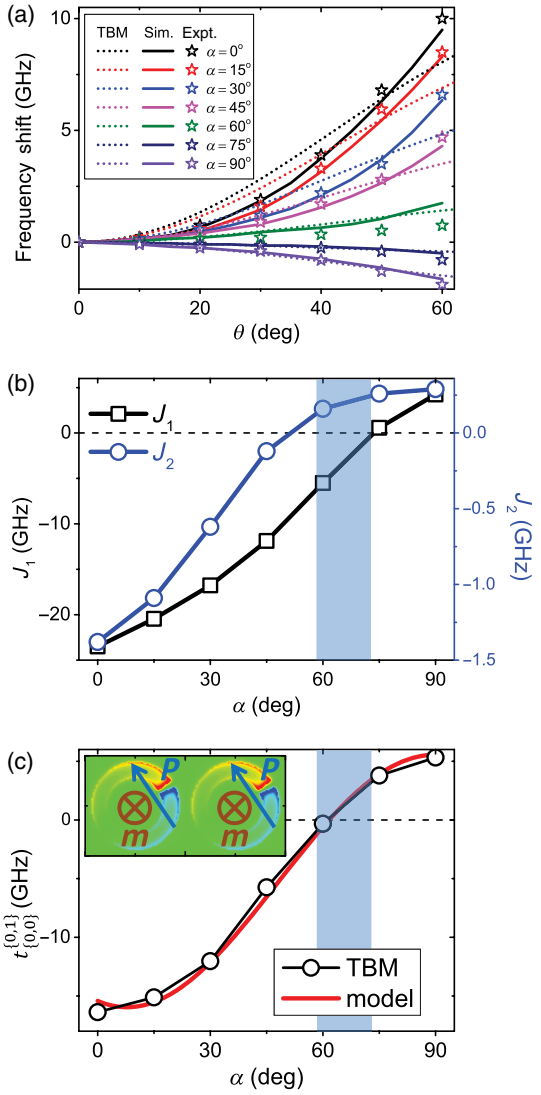

FIG. 3. (a) Resonant frequency shifts versus incident angles for metasurfaces with different values of α obtained through experiments (the stars), FEM simulations (the solid lines), and TBM calculations (the dashed lines). (b) J_1 and J_2 calculated with the TBM for samples with different α values. (c) Nearest-neighbor coupling strength $t_{(0,0)}^{(1,0)}$ as a function of α, obtained through direct TBM calculations (scatters) and through the effective model Eq. (5) (the red line). (Inset) E_z-field distribution on the structure surface calculated with FEM simulations at frequency 0.63 THz.

We now quantitatively compute through Eqs. (1) and (4), the two parameters J_1 and J_2 for metasurfaces with different values of α. Figure 3(b) depicts how the calculated J_1 and J_2 values vary as a function of α. We note that J_1 is roughly 10 times larger than J_2 in most cases, which is reasonable since J_1 represents the nearest-neighbor interrow coupling. Quite as expected, while in the region of $\alpha \to 0°$, both J_1 and J_2 are negative, leading to a positive angular dispersion, they become both positive in the region of $\alpha \to 90°$, which explains the negative angular dispersion found in Figs. 2(e) and 2(f). Of particular interest is that

there exists a critical region [the shaded area in Fig. 3(b)] where J_1 and J_2 successively cross zero, which coincides well with the sign-change angle of the angular dispersion, discovered in Fig. 3(a).

However, J_1 and J_2 are still effective row-row couplings which cannot *directly* reveal the inherent physics. To understand the physics more deeply, we need to sort out the most important terms in determining the angular dispersion. Noting that J_1 is much larger than J_2 [see Fig. 3(b)] and that, obviously, the nearest-neighbor coupling $t_{\{0,0\}}^{\{0,1\}}$ is the leading term in J_1, we examine how $t_{\{0,0\}}^{\{0,1\}}$ varies against α. The computed $t_{\{0,0\}}^{\{0,1\}} \sim \alpha$ relation, depicted in Fig. 3(c) as open circles, indeed has already exhibited the intriguing sign-change behavior in the vicinity of $\alpha = 60°$.

We finally arrive at a position to set up a simple picture to understand the intriguing angular dispersions revealed in Fig. 2. As shown in the inset of Fig. 3(c), a SRR possesses an electric dipole moment $\vec{p}$ and a magnetic dipole moment $\vec{m}$ simultaneously. According to the effective model for plasmonic coupling developed in Refs. [37, 38], the plasmonic coupling strength between two such particles contains four different terms, t_{pp}, t_{mm}, t_{pp}^{rad}, and t_{pm}, representing, respectively, the dipolar interactions for two different types of dipoles, the radiation-correction term, and a cross-interaction term between $\vec{p}$ and $\vec{m}$. In our studied case, while $\vec{m}$ is always along the z direction, the direction of $\vec{p}$ changes as a function of α. Taking this information into consideration, we find from Ref. [38] that the inter-SRR coupling can be effectively rewritten as

$$t_{\mathrm{model}} = A \times \left\{ p^2(1-3\cos^2\alpha) + \left(\frac{m}{c}\right)^2 - p^2(1+\cos^2\alpha)\frac{(k_0 P)^2}{2} - \frac{pm\sin\alpha(k_0 P)}{c} \right\}, \quad (5)$$

with A being a normalization constant. For the lowest resonance mode of a SRR, both p and m can contribute to the coupling strength, and their normalized amplitudes are of the same order (i.e., $p \propto m/c$). To only reveal the physics without involving too many complexities, we fix the ratio between p and m/c as 0.99, based on the finite-difference-time-domain-calculated current distributions in the structure, and choose an appropriate normalization constant $Ap^2 = 6.01$ GHz through a fitting with Fig. 3(c). Inserting these parameters into Eq. (5), we calculate t_{model} as a function of α and then show the results in Fig. 3(c) as a solid line. Excellent agreement is found between the effective-model results and the TBM curve.

Such an effective model reveals the underlying physics clearly. Now our meta-atom exhibits both electric and magnetic dipole moments at its resonance, and the interparticle couplings for two different types of moments display distinct dependences on the parameter α [see Eq. (5)]. It is the competition among the different coupling terms that generates an extraordinary α dependence of the total coupling strength, leading to a sign change of the effective row-row couplings between adjacent SRR arrays, which, in turn, finally results in the intriguing angular dispersions displayed in Fig. 2.

In addition, our approach is also applicable to understanding the dispersion of surface-plasmon polaritons (SPPs) in systems consisting of an array of plasmonic resonators. By controlling the couplings between different resonators, the dispersion of the SPP generated in such systems can be well controlled, yielding various fascinating physical effects, as has already been illustrated in the literature [45–47].

IV. APPLICATIONS

Previous analyses motivate us to propose an alternative strategy to design functional devices. Since the angular dispersion of a metasurface is mainly determined by the plasmonic coupling between two neighboring meta-atoms, we can purposely design relevant microstructures to control the angular dispersion of the metasurface to make it function distinctly when seen at different incidence angles. In what follows, we take a periodic metasurface as an example to show how the strategy works.

As schematically illustrated in Fig. 4(a), we use a metal-insulator-metal (*M-I-M*) structure as the basic meta-atom in designing our multifunctional metadevice. Such *M-I-M* structures have been widely used to realize high-efficiency metadevices in the literature [22,48,49], with functionalities ranging from polarization control to perfect absorption, but these metadevices typically only exhibit *single* functionality since these *periodic homogeneous* metasurfaces (not gradient ones) consist of only one *independent* meta-atom and thus lack design freedom. In the following, we show that, in fact, the angular dispersion can be an additional degree of freedom to offer more functionality to a metasurface, even though the system still consists of only one independent meta-atom.

Our meta-atom is composed by an *x-y isotropic* metallic cross-shaped resonator (consisting of two interconnected metallic **H**-shaped planar resonators) and a continuous metal film separated by a 4-μm-thick dielectric spacer ($\varepsilon_r = 2.25$). We assume that the metallic structures are made by gold films with 1-μm thickness. Since the transmission channel is completely blocked by the metallic film on the bottom, the system must be totally reflective and thus we need to study only the reflection-phase responses (we neglect material losses for simplicity). The solid line in Fig. 4(c) depicts the calculated reflection-phase spectrum of our designed metasurface under normal-incidence excitation, which exhibits a well-defined magnetic resonance [see Fig. 4(b) for the simulated E_z-field distribution of the mode] at $f = 0.54$ THz, with the reflection phase undergoing a 2π variation as the frequency passes through the resonant frequency. Since our meta-atom exhibits a fourfold

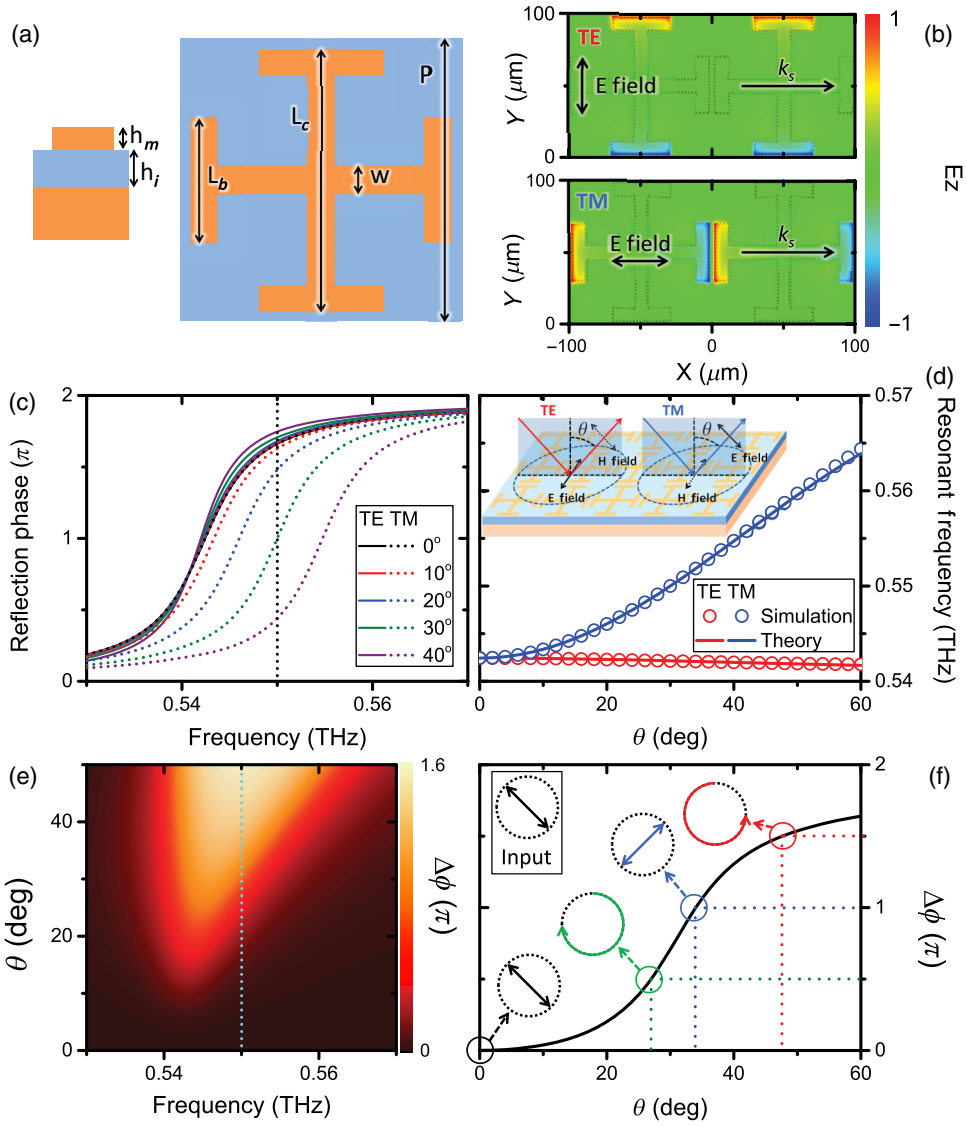

FIG. 4. (a) Side and top views of the designed meta-atom. (b) E_z-field distributions on the structural surfaces in two different cases, obtained with FEM simulations at 0.54 THz under normal incidence. (c) FEM-simulated reflection-phase spectra of the designed metasurface shined by terahertz waves at different incident angles with TE (solid lines) and TM (dotted lines) polarizations. (d) Resonant frequency versus incident angle as the metasurface is shined by oblique incident waves taking TE (red) and TM (blue) polarizations, obtained with FEM simulations (the circles) and theoretical calculations based on the TBM (the solid lines). (e) FEM-simulated reflection-phase difference between TE and TM cases for our metasurface versus incident angle and frequency. (f) TE-TM reflection-phase difference (the solid line) as a function of incident angle, calculated with FEM simulations at 0.55 THz, showing that the reflected beam can exhibit different polarization states if the input wave is linearly polarized as depicted in the inset. The geometrical parameters are $P = 100$ μm, $L_c = 92$ μm, $L_b = 40$ μm, $w = 8$ μm, $h_m = 1$ μm, and $h_i = 4$ μm.

symmetry, it is not surprising to see that the reflection-phase spectra of the metasurface are identical for $\vec{E}\|\hat{x}$ (defined as TE polarization) and $\vec{E}\|\hat{y}$ (TM) polarizations under normal incidence.

As the incidence angle θ varies, we find that the reflection-phase spectra for the two polarizations change in a dramatically different way. As shown in Fig. 4(c), whereas the reflection-phase spectra remain nearly unchanged for the TE incidence (the solid lines), they undergo considerable change for varying values of θ for the TM case (the dotted lines). Because of the distinct θ dependences of the two reflection-phase spectra, the two-cross-polarization phase difference ($\Delta\phi = \phi_{\mathrm{TE}} - \phi_{\mathrm{TM}}$) can be strongly modulated by the incidence angle θ, as shown in Fig. 4(e).

These intriguing results suggest that our device exhibits multiple polarization-control capabilities. Figure 4(f) shows that, at 0.55 THz, the $\Delta\phi$ can be continuously tuned from 0 to 1.55π as the incidence angle θ changes from 0° to 60°. Therefore, assuming that the input wave is linearly polarized and can be decomposed into TE and TM modes with equal amplitudes, the polarization state of the reflected wave can be efficiently controlled by varying the incident angle θ. For example, the polarization state of the reflected beam must be a right-handed circular polarization (RCP) at $\theta = 27°$, but changes to a linear polarization (LP) with **E** perpendicular to its original direction at $\theta = 34°$, and it can be a left-handed circular polarization (LCP) at $\theta = 47.5°$. Other types of polarizations can also be realized at other incident angles or by changing the polarization state of the input beam.

Such dramatic modulations on EM responses of our metasurface are caused by the *controllable* angular dispersions of the device. The red and blue circles in Fig. 4(d) depict the simulated angular dispersions of our metadevice for two different polarizations, showing that, indeed, the TM-mode frequency changes significantly as a function of θ, while the TE mode does not. To understand the physical origins of such intriguing results, we employ the theory

developed in the last section to compute the angular dispersions of the metasurface for different polarizations. Keeping only the nearest-neighbor inter-row coupling term, we find that the angular dispersions can be well described by the formula $f(\theta) = f_0 + J_1\{\cos[Pk_0 \sin(\theta)] - 1\}$, with $f_0 = 0.5424$ THz. We employ the TBM to calculate J_1 for the two cases and find that $J_1 = 1.7$ GHz (TE) and $J_1 = -48.6$ GHz (TM). Putting these results into the above formula, we calculate the mode dispersions for the two polarizations, and we depict the results in Fig. 4(d) by solid lines. Perfect agreement is found between the simulation and our TBM results.

Now the principle to design our multifunctional polarization-control metadevice is very clear. As shown in Fig. 4(b), the EM fields associated with the excited resonance mode on the meta-atom are localized mainly around two metallic bars. In the TE case under study, the plasmonic coupling dictating the angular dispersion is due mainly to that between two nearest-neighbor meta-atoms placed along the x direction. Since the hot spots in two meta-atoms are far away, they do not have strong contributions to the coupling, which explains why the TE mode shows negligible angular dispersion [see Fig. 4(b)]. However, things are completely different for the TM case where the resonance field pattern is rotated by 90°. Still considering the plasmonic couplings between the same two meta-atoms, in this TM case, the EM fields of the two resonance modes strongly overlap with each other, leading to a much stronger coupling coefficient. It is the difference in plasmonic couplings along the different directions that generates the distinct angular dispersions for the two polarizations, which eventually offers the device very rich polarization-control capabilities for input waves coming from different angles.

V. CONCLUSIONS

To summarize, we establish in this paper a theoretical framework to study the angular dispersions in periodic metasurfaces, and we validate the theory with terahertz experiments on a metasurface exhibiting opposing angular dispersions for the two polarizations. Our analyses reveal the important role of plasmonic near-field coupling in dictating the angular dispersions in metasurfaces, which can be utilized as an additional degree of freedom to design multifunctional metadevices. As an illustration, we design a multifunctional terahertz polarization controller, which can realize distinct polarization-manipulation functionalities at different incident angles. Our findings significantly expand the capabilities of the metasurface in manipulating EM waves and can stimulate high-performance multifunctional metadevices for practical applications. Extending the concept to designing inhomogeneous gradient metasurfaces with impinging-angle-dependent multifunctionalities would be of interest for future projects, particularly at high frequencies (e.g., infrared and optical frequencies).

ACKNOWLEDGMENTS

This work was supported by National Key Research and Development Program of China (Grants No. 2017YFA0303504 and No. 2017YFA0700201), the National Natural Science Foundation of China (Grants No. 11734007, No. 11474057, and No. 11674068), and the Natural Science Foundation of Shanghai (Grants No. 16ZR1445200, No. 16JC1403100, and No. 18ZR1403400). Part of experimental works was carried out in Fudan Nanofabrication Laboratory.

[1] N. Yu and F. Capasso, Flat optics with designer metasurfaces, Nat. Mater. **13**, 139 (2014).
[2] H.-H. Hsaio, C. H. Chu, and D. P. Tsai, Fundamentals and applications of metasurfaces, Small Methods **1**, 1600064 (2017).
[3] J. Hao, Y. Yuan, L. Ran, T. Jiang, J. Kong, C. Chan, and L. Zhou, Manipulating Electromagnetic Wave Polarizations by Anisotropic Metamaterials, Phys. Rev. Lett. **99**, 063908 (2007).
[4] S.-C. Jiang, X. Xiong, Y.-S. Hu, Y.-H. Hu, G.-B. Ma, R.-W. Peng, C. Sun, and M. Wang, Controlling the Polarization State of Light with a Dispersion-Free Metastructure, Phys. Rev. X **4**, 021026 (2014).
[5] T. Li, H. Liu, S. M. Wang, X. G. Yin, F. M. Wang, S. N. Zhu, and X. Zhang, Manipulating optical rotation in extraordinary transmission by hybrid plasmonic excitations, Appl. Phys. Lett. **93**, 021110 (2008).
[6] L. Cong, N. Xu, J. Gu, R. Singh, J. Han, and W. Zhang, Highly flexible broadband terahertz metamaterial quarter-wave plate, Laser Photonics Rev. **8**, 626 (2014).
[7] C. Huang, Y. Feng, J. Zhao, Z. Wang, and T. Jiang, Asymmetric electromagnetic wave transmission of linear polarization via polarization conversion through chiral metamaterial structures, Phys. Rev. B **85**, 195131 (2012).
[8] S. Wu, Z. Zhang, Y. Zhang, K. Zhang, L. Zhou, X. Zhang, and Y. Zhu, Enhanced Rotation of the Polarization of a Light Beam Transmitted through a Silver Film with an Array of Perforated S-Shaped Holes, Phys. Rev. Lett. **110**, 207401 (2013).
[9] N. Liu, M. Mesch, T. Weiss, M. Hentschel, and H. Giessen, Infrared perfect absorber and its application as plasmonic sensor, Nano Lett. **10**, 2342 (2010).
[10] J. Hao, J. Wang, X. Liu, W. J. Padilla, L. Zhou, and M. Qiu, High performance optical absorber based on a plasmonic metamaterial, Appl. Phys. Lett. **96**, 251104 (2010).
[11] X. Xiong, S. C. Jiang, Y. H. Hu, R. W. Peng, and M. Wang, Structured metal film as a perfect absorber, Adv. Mater. **25**, 3994 (2013).
[12] X. Shen, T. J. Cui, J. Zhao, H. F. Ma, W. X. Jiang, and H. Li, Polarization-independent wide-angle triple-band metamaterial absorber, Opt. Express **19**, 9401 (2011).
[13] Y. Yang, I. I. Kravchenko, D. P. Briggs, and J. Valentine, All-dielectric metasurface analogue of electromagnetically induced transparency, Nat. Commun. **5**, 5753 (2014).

[14] L. Zhou, W. Wen, C. T. Chan, and P. Sheng, Electromagnetic-Wave Tunneling through Negative-Permittivity Media with High Magnetic Fields, Phys. Rev. Lett. **94**, 243905 (2005).

[15] Z. Song, Q. He, S. Xiao, and L. Zhou, Making a continuous metal film transparent via scattering cancellations, Appl. Phys. Lett. **101**, 181110 (2012).

[16] J. Hao, C.-W. Qiu, M. Qiu, and S. Zouhdi, Design of an ultrathin broadband transparent and high-conductive screen using plasmonic nanostructures, Opt. Lett. **37**, 4955 (2012).

[17] N. Arju, T. Ma, A. Khanikaev, D. Purtseladze, and G. Shvets, Optical Realization of Double-Continuum Fano Interference and Coherent Control in Plasmonic Metasurfaces, Phys. Rev. Lett. **114**, 237403 (2015).

[18] M. Manjappa, S. Y. Chiam, L. Cong, A. A. Bettiol, W. Zhang, and R. Singh, Tailoring the slow light behavior in terahertz metasurfaces, Appl. Phys. Lett. **106**, 181101 (2015).

[19] B. Zeng, X. Hong, H. S. Jung, A. Zettl, M. F. Crommie, and F. Wang, Optimizing broadband terahertz modulation with hybrid graphene/metasurface structures, Nano Lett. **15**, 372 (2015).

[20] N. Yu, P. Genevet, M. A. Kats, F. Aieta, J.-P. Tetienne, F. Capasso, and Z. Gaburro, Light propagation with phase discontinuities: Generalized laws of reflection and refraction, Science **334**, 333 (2011).

[21] X. Ni, N. K. Emani, A. V. Kildishev, A. Boltasseva, and V. M. Shalaev, Broadband light bending with plasmonic nanoantennas, Science **335**, 427 (2012).

[22] S. Sun, Q. He, S. Xiao, Q. Xu, X. Li, and L. Zhou, Gradient-index meta-surfaces as a bridge linking propagating waves and surface waves, Nat. Mater. **11**, 426 (2012).

[23] A. Pors, M. G. Nielsen, T. Bernardin, J.-C. Weeber, and S. I. Bozhevolnyi, Efficient unidirectional polarization-controlled excitation of surface plasmon polaritons, Light Sci. Appl. **3**, e197 (2014).

[24] G. Zheng, H. Mühlenbernd, M. Kenney, G. Li, T. Zentgraf, and S. Zhang, Metasurface holograms reaching 80% efficiency, Nat. Nanotechnol. **10**, 308 (2015).

[25] M. Khorasaninejad, W. T. Chen, R. C. Devlin, J. Oh, A. Y. Zhu, and F. Capasso, Metalenses at visible wavelengths: Diffraction-limited focusing and subwavelength resolution imaging, Science **352**, 1190 (2016).

[26] Y. Yang, W. Wang, P. Moitra, I. I. Kravchenko, D. P. Briggs, and J. Valentine, Dielectric meta-reflectarray for broadband linear polarization conversion and optical vortex generation, Nano Lett. **14**, 1394 (2014).

[27] X. Yin, Z. Ye, J. Rho, Y. Wang, and X. Zhang, Photonic spin Hall effect at metasurfaces, Science **339**, 1405 (2013).

[28] B. Zhang, Y. Zhao, Q. Hao, B. Kiraly, I.-C. Khoo, S. Chen, and T. J. Huang, Polarization-independent dual-band infrared perfect absorber based on a metal-dielectric-metal elliptical nanodisk array, Opt. Express **19**, 15221 (2011).

[29] A. Di Falco, Y. Zhao, and A. Alú, Optical metasurfaces with robust angular response on flexible substrates, Appl. Phys. Lett. **99**, 163110 (2011).

[30] R. Alaee, M. Farhat, C. Rockstuhl, and F. Lederer, A perfect absorber made of a graphene micro-ribbon metamaterial, Opt. Express **20**, 28017 (2012).

[31] Y. Huang, Q. Zhao, S. K. Kalyoncu, R. Torun, Y. Lu, F. Capolino, and O. Boyraz, Phase-gradient gap-plasmon metasurface based blazed grating for real time dispersive imaging, Appl. Phys. Lett. **104**, 161106 (2014).

[32] F. Aieta, M. A. Kats, P. Genevet, and F. Capasso, Multi-wavelength achromatic metasurfaces by dispersive phase compensation, Science **347**, 1342 (2015).

[33] B. Xi, H. Xu, S. Xiao, and L. Zhou, Theory of coupling in dispersive photonic systems, Phys. Rev. B **83**, 165115 (2011).

[34] J. B. Pendry, A. J. Holden, D. J. Robbins, and W. J. Stewart, Magnetism from conductors and enhanced nonlinear phenomena, IEEE Trans. Microwave Theory Tech. **47**, 2075 (1999).

[35] L. Zhou and S. T. Chui, Eigenmodes of metallic ring systems: A rigorous approach, Phys. Rev. B **74**, 035419 (2006).

[36] L. Zhou, X. Huang, Y. Zhang, and S.-T. Chui, Resonance properties of metallic ring systems, Mater. Today **12**, 52 (2009).

[37] M. Qiu, S. Xiao, Q. He, S. Sun, and L. Zhou, Experimental verifications on an effective model for photonic coupling, Opt. Lett. **40**, 272 (2015).

[38] B. Xi, M. Qiu, S. Xiao, H. Xu, and L. Zhou, Effective model for plasmonic coupling: A rigorous derivation, Phys. Rev. B **89**, 035110 (2014).

[39] See Supplemental Material at http://link.aps.org/supplemental/10.1103/PhysRevApplied.9.054050 for the simulation and experimental results of all of the samples besides Figs. 2(e) and 2(f).

[40] COMSOL, Inc., COMSOL MULTIPHYSICS, version 3.5, 2008.

[41] A. Raman and S. Fan, Photonic Band Structure of Dispersive Metamaterials Formulated as a Hermitian Eigenvalue Problem, Phys. Rev. Lett. **104**, 087401 (2010).

[42] N. W. Ashcroft and N. D. Mermin, *Solid State Physics*, College Edition (Harcourt College Publishers, New York, 1976).

[43] S. Pandey, B. Gupta, A. Chanana, and A. Nahata, Non-Drude like behaviour of metals in the terahertz spectral range, Adv. Phys. X **1**, 176 (2016).

[44] We use Bloch boundary conditions and plane-wave input in our simulations. The dielectric constant for gold in the terahertz regime is obtained from Ref. [41], and the one for the quartz substrate is 2.96.

[45] A. A. High, R. C. Devlin, A. Dibos, M. Polking, D. S. Wild, J. Perczel, N. P. de Leon, M. D. Lukin, and H. Park, Visible-frequency hyperbolic metasurface, Nature (London) **522**, 192 (2015).

[46] D. Correas-Serrano, A. Alù, and J. S. Gomez-Diaz, Plasmon canalization and tunneling over anisotropic metasurfaces, Phys. Rev. B **96**, 075436 (2017).

[47] A. Nemilentsau, T. Low, and G. Hanson, Anisotropic 2D Materials for Tunable Hyperbolic Plasmonics, Phys. Rev. Lett. **116**, 066804 (2016).

[48] W. Luo, S. Xiao, Q. He, S. Sun, and L. Zhou, Photonic spin Hall effect with nearly 100% efficiency, Adv. Opt. Mater. **3**, 1102 (2015).

[49] X. Li, S. Xiao, B. Cai, Q. He, T. J. Cui, and L. Zhou, Flat metasurfaces to focus electromagnetic waves in reflection geometry, Opt. Lett. **37**, 4940 (2012).